First-principles calculations of metal surfaces. II. Properties of low-index platinum surfaces toward understanding electron emission

Peter A. Schultz,* Harold P. Hjalmarson, Morgann Berg, Ezra Bussmann, David A. Scrymgeour, Taisuke Ohta, and Chris H. Moore

Sandia National Laboratories, Albuquerque, New Mexico 87185, USA

(Received 9 January 2021; revised 27 April 2021; accepted 5 May 2021; published 20 May 2021)

The stability of low-index platinum surfaces and their electronic properties is investigated with density functional theory, toward the goal of understanding the surface structure and electron emission, and identifying precursors to electrical breakdown, on nonideal platinum surfaces. Propensity for electron emission can be related to a local work function, which, in turn, is intimately dependent on the local surface structure. The $(1 \times N)$ missing row reconstruction of the Pt(110) surface is systematically examined. The (1×3) missing row reconstruction is found to be the lowest in energy, with the (1×2) and (1×4) slightly less stable. In the limit of large $(1 \times N)$ with wider (111) nanoterraces, the energy accurately approaches the asymptotic limit of the infinite Pt(111) surface. This suggests a local energetic stability of narrow (111) nanoterraces on free Pt surfaces that could be a common structural feature in the complex surface morphologies, leading to work functions consistent with those on thermally grown Pt substrates.

DOI: 10.1103/PhysRevB.103.195427

I. INTRODUCTION

Field emission and electrical breakdown at real metal surfaces are complex phenomena at the heart of the operation of many electronic devices. The fundamental understanding of field emission as a prerequisite to vacuum breakdown remains in its infancy. The principal working understanding of emission at surfaces is captured in the empirical Fowler Nordheim relation [1–4]

$$J(E, \phi, \beta) = \frac{A\beta^2 E^2}{\phi} \exp\left(\frac{B\phi^{3/2}}{\beta E}\right), \tag{1}$$

where the functional dependency of the emission current density J in Eq. (1) on the field E, work function ϕ, and an empirical structural enhancement factor β is isolated from other factors (subsumed into constants A, B). The vital role of the work function in local emission is indicated by its presence in the exponential (as well as in the prefactor). The work function is directly dependent upon the structure. Moreover this overall emission has an empirical fitting parameter β related to structural effects (e.g., from field enhancement at protuberances at the surface) and can vary several orders of magnitude, up to 1000, inside the exponential. To understand electrical breakdown at real—i.e., nonideal, thermally grown, polycrystalline—surfaces will require relating growth process to the resulting surface structure, and relating features to effective local work functions, and ultimately to emission and breakdown. A goal of this paper is to seek first-principles understanding of the relationship of surface structure and electronic properties, motivated by the desire to gain insight into the surfaces features leading to electron emission experimentally observed at "real" metal surfaces [5].

Platinum is a noble metal that adopts the fcc crystal structure. Yet despite adopting the simplest of crystal structures, each of the ideal low-index platinum surfaces exhibits a surprising amount of complexity. The ideal (100) surface reconstructs to form a quasihexagonal overlayer [6–8]. The more open (110) surface reconfigures to a "missing row" reconstruction composed of alternating tilted (111) nanoterraces [9–11]. The (111) surface—the close-packed hexagonal surface that is the lowest-energy surface under ideal conditions—is only itself marginally stable, a large tensile stress in the surface making addition of atoms into the surfaces nearly favored [12]. Elevated temperatures (above 1330 K) trigger reconstruction to a denser yet (near-)hexagonal overlayer incommensurate with the bulk-terminated hexagonal layer [6,13–15]. The increased chemical potential of Pt in gas-phase deposition also induces reconstruction, that remains stable below 700 K [16]. Even the "simple" surfaces of platinum are not simple.

In this paper we seek to understand the properties of real platinum surfaces, to comprehend the local surface structure, correlate with local work functions, and thereby connect to electron emission behavior. Using density functional theory (DFT), we examine the ground state structures of low-index platinum surfaces, using a slab-consistent reference method that enables fine-accuracy comparisons of different surface models to resolve different surface reconstructions. In particular, we investigate $(1 \times N)$ missing row reconstructions of the (110) surfaces. Noting an homologous mapping from the (110) surface to a (111) surface in the narrow and wide limits of a missing row reconstruction, we find that a (1×3) structure is the lowest energy reconstruction, and that energy steadily increases with large N [and wider (111) terraces] toward the

*paschul@sandia.gov

asymptotic limit of the (111) surface energy. The local stability of narrower (111) nanoterraces indicates that these are likely common features on a free Pt surface contributing to the complex surface morphology observed in the experiments [5]. Comparisons of the work functions computed from these missing row models to the experiment are consistent with this picture.

The next section presents representative experimental results for thin-film Pt surfaces grown by sputtering, summarizes other intriguing experimental literature concerning grown Pt surfaces. The following section describes the computation setup: the methods, choice of functionals, and the design of the slab model for the surface calculations, taking advantage of a new method for extracting convergent surface properties using slab-consistent bulk reference energies [17]. The body of the paper describes the results for the Pt surfaces, culminating with emphasis on designing accurate discriminating models for (110) surface reconstructions. We close with a discussion of implications of the results for understanding electron emission from real platinum surfaces and a final section to conclude.

II. PLATINUM SURFACE CHARACTERIZATION

To develop a comprehensive understanding of surface morphology and correlation of local features of that morphology to work functions and electron emission, we begin with an experimental examination of a sputter-deposited, polycrystalline (poly-Pt) thin film using a set of surface characterization tools. The thin films were fabricated on substrate consisting of a 40 nm ZnO adhesion layer sputtered onto 400 nm of thermal a-SiO_2 on Si(100), following a procedure outlined in Ref. [18]. Onto this substrate, 90 nm of Pt was sputtered and annealed in air at 900 °C, which created a polycrystalline microstructure. Greater elaboration of the surface characterization techniques and a more detailed analysis of the results is presented elsewhere [5], just the salient intriguing features are presented here.

These sputtered Pt thin films are polycrystalline, with grain sizes a few 100 nm. The Pt grains at the poly-Pt surface exhibited a local crystallographic orientation, as determined from EBSD (electron backscattered diffraction) measurements, that was predominately (111)-oriented normal to the surface, to within a few degrees. The overall complexity of this surface is revealed in an AFM (atomic force microscopy) topograph of a typical Pt film depicted in Fig. 1. While optically smooth, the AFM topograph measures a surface roughness of several tens of nm, despite the near-(111) orientation of all the substrate grains.

The measured spatial variation in the local work function is shown in Fig. 2. The PEEM measurement in Fig. 2(a) mimics the spatial variability observed in the AFM topograph in Fig. 1.

The analysis of the work function in Fig. 2(b) shows the work function distribution has modest variation centered around 5.7(±0.2) eV. This is far short of the 6.1 eV observed for the work function of the flat (111) surface on a single crystal Pt [19], indicating that electron emission from the surface is dominated by features other than large (111) facets,

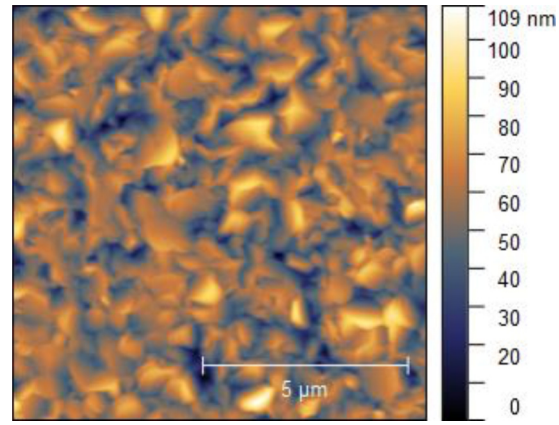

FIG. 1. AFM topograph of a representative polycrystalline (111)-oriented Pt surface.

to within the resolution of the technique [few tens of nm per pixel in Fig. 2(a)].

Previous experiments documented further unusual behavior for growth on Pt(111)-oriented substrates. Kalf *et al.* [20] observed the growth of stepped triangular pyramids in STM images of homoepitaxy on Pt(111), rather than pyramids with extensive (111) faces. This observation was echoed in later studies of thermal growth that showed roughly triangular hillocks [21], hillocks stacked with a (111) orientation [22].

Kalff had proposed that this growth was a natural consequence of adsorption growth kinetics [20] that the stepped pyramidal structure emerged directly from kinetic Monte Carlo studies as a balance between surface diffusion barriers and a step-hop barrier. In the computational analysis below, we will argue that local energetic considerations might also contribute to the growth and persistence of this stepped morphology.

III. COMPUTATIONAL CHALLENGES

Density functional theory (DFT) calculations are the state-of-the-art approach for modeling physical properties of surfaces, such as atomic structural relaxations and surface reconstructions, and electronic properties such as work functions. Slab calculations of thin metal films within a supercell approximation are used to model semi-infinite surfaces. A model slab has two surfaces separated by a discrete number of atomic layers, equivalent to a semi-infinite surface in the limit of infinitely thick slabs.

Methods to extract surface properties from these slab models evolved over the course of nearly three decades [23–27]. In previous work [17] we have developed an improved protocol based upon meticulously consistent levels of standard accuracy between bulk and slab surface calculations that proves to give faster, more reliable convergence of surface energies with slab thickness, and thus greater accuracy at much reduced computational cost.

Platinum surfaces have been a staple of surface science studies for decades. Being a noble metal that crystallizes into an fcc structure, platinum surfaces are relatively chemically stable and easy to prepare. Simultaneously, the Pt surface has been the subject of numerous computational studies, included

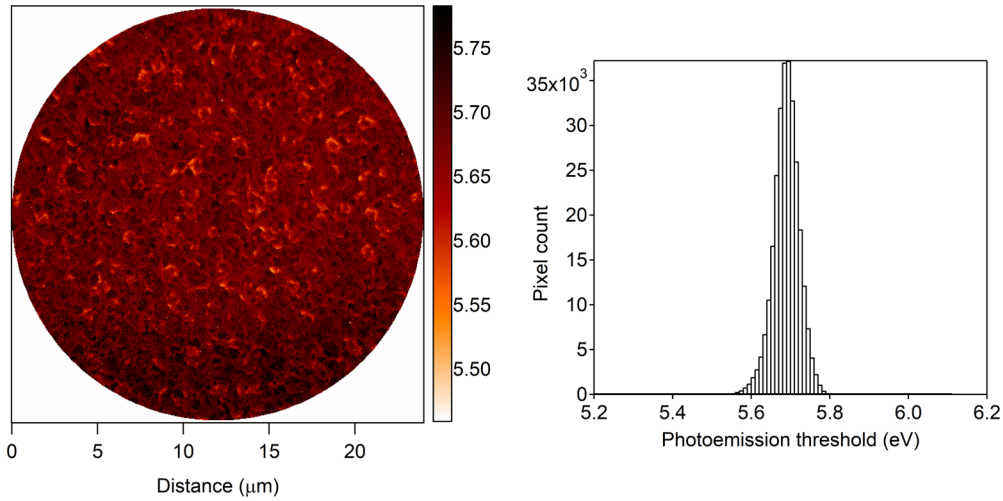

FIG. 2. PEEM measurements of a representative Pt polycrystalline thin film: (note: not the same location as the AFM topograph of Fig. 1). (a) PEEM measurement of the local work function across the surface; and (b) histogram of recorded local work functions.

as an examplar in foundation surface methods studies using DFT, such as Singh-Miller and Marzari [27]. Properties of more complex surfaces, e.g., relative energetics of potential reconstructions from ideal bulk termination, are less well studied, as are phenomena that govern evolution of surface structure. Feibelman studied such processes as the energetics of steps on Pt(111) surfaces [28] or diffusion of Pt atoms on the Pt(111) and over steps [29]. To gain insight into complex morphologies of grown surfaces entails a more focused investigation of surface reconstructions, requiring systematic investigation of large-area reconstructions with precise relative accuracy.

IV. COMPUTATIONAL METHODS

The DFT calculations in this work were performed with the SEQQUEST code [30], a pseudopotential DFT code using linear combinations of carefully optimized contracted Gaussian basis sets to represent the electronic wave functions. The local orbital basis with explicit use of range cutoffs proves advantageous at enforcing boundary conditions in systems with reduced dimensionality (such as slab models of surfaces).

The Pt atoms in the calculation are represented by a ten-valence-electron pseudopotential generated within Hamann's generalized norm-conserving pseudopotential (GNCPP) formalism [31], using the GNCPP code to generate the LDA pseudopotential and the FHI98PP code [32] for all other functionals. The 5*d* and 6*s*-6*p* shells are treated as valence electrons, relegating the 5*s*-5*p* semicore electrons to status as core electrons treated implicitly by the pseudopotential. A nonlinear core correction (NLCC) [33] is incorporated into the pseudopotential to take into account the remnant exchange-correlation effects between these semicore electrons and the valence elections, necessary to avoid a spurious magnetism in fcc Pt that occurs using standard pseudopotentials.

The platinum atom basis set is a carefully optimized "double-zeta plus polarization" (DZP) contracted Gaussian basis, providing two radial degrees of freedom for the strongly occupied *s* and *d* orbitals, plus a single radial function for the weakly occupied *p* shell to allow for angular polarization. A known challenge for atom-centered local orbital basis sets (cf. plane wave methods) in metals is accurately describing the long-range fall-off of the electron density into vacuum at the surface, particularly crucial to obtain convergent work functions. To remedy this, we augment this Pt atomic-centered basis with a set of "floating orbitals" on the surface, in the first set of vacant sites above the surface atoms. The ghost atom basis has *s*, *p*, and *d* orbitals consisting of a single diffuse Gaussian each, decay constant 0.08, 0.12, and 0.16 bohr^{-2}, respectively. The adequacy of this procedure is verified in direct tests comparing work functions (below).

The Pt surface calculations used several flavors of density functionals:

(1) The local density approximation (LDA) as parametrized by Perdew and Zunger [34]—empirically observed to give better surface properties than generalized gradient approximations.

(2) The generalized gradient approximation as formulated by Perdew, Burke, and Ernzerhof (PBE) [35]—usually better for bulk properties of transition metals such as Pt.

(3) The AM05 functional created by Armiento and Mattsson [36] using a subsystem functional approach—specifically devised to improve the treatment of an evanescent density such as that outside a surface.

The LDA and PBE have been commonly used in DFT studies of metals and metal surfaces, and are included here to provide verification benchmarks against previous Pt surface studies (such and Singh-Miller and Marzari [27]). The principal results in this study use the AM05, as it has specifically been designed to eliminate surface errors present in standard functionals (such as LDA and PBE).

The occupation of electronic states near the Fermi level is smeared using a Fermi function fill factor. An (artificial) electronic temperature of 0.003 Ryd (~41 meV) is used to smear the occupations near the Fermi level. Cognizant of the perils of using smearing methods [37,38], errors that are likely to be exacerbated at the surface (in occupying states above the Fermi level), this temperature is set just large enough to achieve electronic self-consistency (up to a slab thickness of

TABLE I. Computed bulk properties of platinum: lattice parameters a_0 (Å) and bulk modulus B (GPa).

	LDA		PBE		AM05	
	a_0	B	a_0	B	a_0	B
This work	3.894	310	3.969	253	3.928	284
With NLCC	3.909	305	3.985	243	3.925	280
Ref. [45]	3.909	–	3.985	–	3.923	–
Ref. [46]	3.894	312	3.971	247	–	–
Ref. [26]	3.89	312	3.97	241	–	–
Ref. [27]	–	–	3.99	246	–	–
Experiment (0 K)		3.916 Å [43]	288 GPa [44]			

~40 layers), but smaller than a temperature that significantly affects the electronic structure and might otherwise unacceptably begin to corrupt results [38] for surface energies and work functions.

The slab models for the simple low-index surfaces start with a central layer in the middle of the slab, and incrementally add an atomic layer on both sides of the slab to create total slabs with an off number of layers. The slabs are separated with sufficient vacuum ($\geqslant$10 Å) to isolate the periodic slabs from one another (the SEQQUEST code explicitly enforces this isolation, checking for any overlap of slab density with the vacuum boundary), and the slab and the vacuum boundary are deliberately aligned to enable exactly consistent conditions for the slab and bulk to obtain an accurate slab-consistent bulk reference [17]. Atom positions are relaxed to minimum energy configurations (ghost atoms are held fixed to bulk terminated positions), using all available symmetry, adapting for geometry updates a modified Broyden method due to Johnson [39]. An atomic relaxation is deemed converged when the total force on every atom is less than 0.0002 Ryd/bohr (5 meV/Å). The positions of ghost atoms are not optimized. The energy gains are minuscule, and including these ghost atoms in the full relaxation to resolve their (somewhat noisy) small forces needlessly degrades the overall convergence, for minimal benefit.

V. RESULTS AND ANALYSIS

A. Bulk properties of fcc platinum

Bulk crystal properties of fcc Pt obtained with this computational setup are presented in Table I. The computed lattice constant a_0 and bulk modulus B are shown, compared to previous computational literature to verify the adequacy of the computational methods used here and compared to experiment to validate that the DFT provides adequate physical accuracy. The lattice parameter and bulk modulus are obtained from a (cubic polynomial) fit using a Birch-Murnaghan equation of state [40–42]. Setting aside the artificial electronic temperature, all the calculations are 0 K DFT calculations, so that the appropriate comparisons are to experimental properties extrapolated to 0 K: the 0 K lattice constant is 3.916 Å [43] and bulk modulus is 288 GPa [44].

The near-exact agreement of our local-orbital pseudopotential results with all-electron FLAPW (full-potential linear augmented plane wave) benchmarks [45,46] verifies the quality of the pseudopotentials (replacement of the explicit core electrons with a nonlinear core-corrected effective core potential) and the local basis (rather than a larger, more flexible plane wave basis). Our results also agree well with the bulk results for previous work on Pt surface calculations [26,27], indicating that later comparisons of the results for surface calculations will be meaningful. The agreement of our results with different FLAPW results—the widely acknowledged benchmark of DFT—is better than the agreement between different FLAPW calculations with each other, and better than the differences between any of the DFT calculations and experiment.

The differences between the standard and NLCC pseudopotential results are small, and not physically significant. Nonetheless, we use the NLCC in the following. Without the NLCC, the standard pseudopotentials spuriously yield magnetic fcc platinum (ferromagnetic with 0.38 μ_B/Pt is 5 meV/Pt lower than paramagnetic platinum with the LDA, 0.53 μ_B is 25 meV lower with PBE, and 0.57 μ_B is 15 meV lower with AM05), whereas the NLCC correction correctly predicts paramagnetic fcc Pt. While we do not consider spin polarization in this clean surface study, a follow-up study might undertake to investigate atomic/molecular adsorption chemistry on Pt surfaces, and a spurious magnetism would corrupt those analyses.

The agreement of our current results with experiment, for the lattice constant and bulk modulus, using both the standard and nonlinear core-corrected pseudopotentials is very good, typical for these DFT functionals. The values we present are k-limit results, i.e., results extrapolated to infinite k sampling as an average of results using 17^3 to 24^3 k grids (where most literature work deems a 16^3 grid to be converged). In addition to AM05's more intrinsically accurate treatment of surface effects [36], AM05 also has shown greater accuracy in predicting bulk properties [47]. As seen in Table I, it outperforms LDA and PBE for fcc Pt, providing additional impetus for using the AM05 to investigate structural properties of Pt surfaces in this study.

B. Low-index platinum surfaces

It has been observed previously [26] that platinum surfaces undergo only small relaxations (<0.1 eV). Without known exception in the literature, the relaxations on low-index fcc metal surfaces attenuate rapidly with distance from the surface, typically diminishing to negligible relaxations within 2–3 layers. This feature is operationally convenient, enabling thinner slab models for surface studies, e.g., earlier studies of

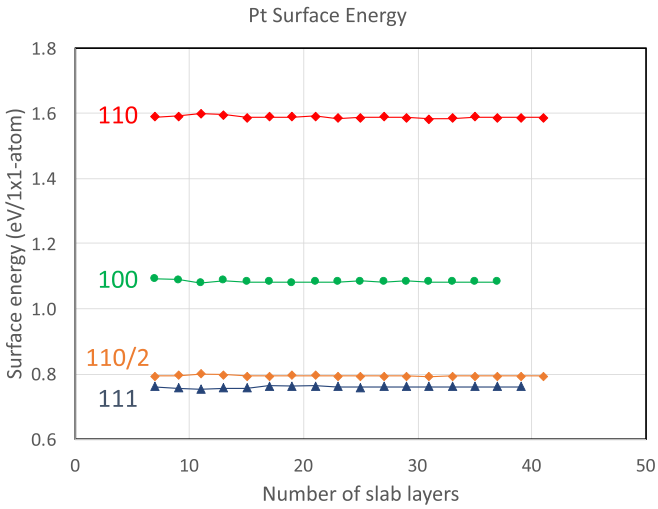

FIG. 3. Computed surface energy for low-index platinum surfaces as a function of slab thickness, in eV/(1 × 1) atom. Lines are only to guide the eye. The 110 result is repeated, counting 2 atoms per (1 × 1) surface cell, showing a close correspondence with the 111. This will be useful in interpreting the 110 missing row reconstruction in the limit of large N.

Pt surfaces used only 7 layers (the FLAPW study of Da Silva *et al.* [26]) or at most 13 layers (the pseudopotential study of Singh-Miller and Marzari [27]). In our platinum surfaces we verified that an all-atom-relaxed slab gave results nearly indistinguishable from slab calculations with only the top four layers at each surface relaxed, in test calculations up to 17 layer slabs. Hence, in what follows, only the top four Pt layers are relaxed, keeping the underlying layers (and the layer of ghost atoms above the surface) fixed to their bulk positions.

Figure 3 shows the computed AM05 surface energy of the unreconstructed, relaxed low-index (110), (100), and (111) platinum surfaces, obtained using the surface-consistent bulk reference energy approach [17], as a function of slab thickness. In this plot, a surface k grid of 12×12 was used for the (100) and (111) surfaces, and 17×12 for the (110).

The accuracy of the slab-consistent bulk reference in computing the surface energy is immediately evident: an error δE^{bulk} in the bulk reference energy would manifest as an N×δE^{bulk} monotonic drift in the surface energy as function of slab thickness. Using a single bulk-computed reference energy for each surface, the computed surface energy is flat out to at least 40 layers, without any extrapolative fitting of the surface energy.

Moreover, for Pt at least, the surface energies are well converged after seven or perhaps nine layers. This proves computationally advantageous (convenient) in our later calculations of Pt(110) reconstructions. The work function has previous been noted to converge even more quickly with slab thickness [24,48]. We documented similar behavior in systematic tests for Al in the first part of this work [17].

The benefit of a reliable slab-consistent bulk reference becomes obvious when one considers that the computed surface energies are well converged with rather coarse (and computationally less intensive) surface k samples. This full surface series was computed with k grids from 6×6 through 16×16 for the Pt(100) and Pt(111), and from 4×6 through 12×17 for the Pt(110) surface. The surface energy converges to within 0.01 eV for the (100) surface with a rather coarse 8×8 k grid, within 0.02 eV for the Pt(111) with 8×8, and within 0.01 eV for the Pt(110) surface with 6×8. The work functions exhibit comparable convergence, e.g., the Pt(111) Φ deviates at most 0.05 eV.

This convergence is achieved without invoking very fine accuracy independently in both bulk and slab calculations. Using extrapolation methods, Da Silva *et al.* [26] required at least 12×12 grids—more than twice as dense—to achieve comparable convergence. What is necessary is that the bulk and surface be explicitly and meticulously consistent so as to have detailed equivalence in their accuracy (with the caveat that the k sampling cannot be so coarse as to significantly degrade the computed bulk lattice constant [17]).

Table II summarizes the converged results from this work for the computed surface energy and the work function for the low-index surface of Pt, and compares this to previous works and to available experiment. These results agree well with the previous results from Da Silva *et al.* (DS) [26] and Singh-Miller and Marzari (SM) [27] at least as well as these previous results agree with each other. We use NLCC-corrected pseudopotentials where SM do not, and we quote k-limit and slab-limit converged results, where DS and SM quote results for smaller 7-layer and 13-layer slabs with a single fixed k-point sampling, so small differences are inevitable. This result verifies the fine numerical accuracy of the current approach, and, in particular, verifies the efficacy of using floating orbitals to eliminate basis set incompleteness errors in the local orbital basis at the surface, even in complex surface configurations [52].

These results constitute our baseline attempt to understand the surface morphology and the consequent variability in the work function exhibited in the experimental measurements of Figs. 1 and 2.

C. Pt(110) missing row reconstructions

As noted above, each of the low-index platinum surfaces reconstruct. The (110) is the focus of this study. The Pt(110) has been observed to undergo missing row reconstructions, and only exhibit the primitive ideal (1 × 1) structure at high temperatures [9–11]. Both a (1 × 2) and (1 × 3) missing row reconstruction has been observed [9,10] and characterized [53–55]. Unresolved questions about the role of impurities in the relative stabilities of these smaller missing row reconstructions continued to be debated, even while a closely related family of higher order (1 × 5), (1 × 7), (1 × 9) reconstructions were observed, and attributed to composites of (1 × 3) + n(1 × 2) missing row reconstructions intermediate between the monolithic (1 × 3) and (1 × 2) missing row reconstructions [56].

Figure 4(a) depicts the simplest (1 × 2) missing row reconstruction, both in side view (along the direction of the missing rows) and top view, where the missing atoms [with respect to the ideal (1 × 1) surface] are indicated by hollowed dashed atoms. For the (1 × 3) missing row reconstruction shown in Fig. 4(b), the ridges (troughs) become taller (deeper) and the terraces become wider. The (111)-oriented nanoterraces

TABLE II. Computed surface energy σ [eV/(1 × 1) surface atom] and work function Φ (eV) for unreconstructed low-index Pt surfaces.

	Pt(111)		Pt(100)		Pt(110)	
	σ	Φ	σ	Φ	σ	Φ
			LDA			
This work	0.86	6.14	1.20	6.12	1.78	5.71
Da Silva (Ref. [26])	0.91	6.06	–	–	–	–
			PBE			
This work	0.67	5.79	0.95	5.74	1.40	5.35
Da Silva (Ref. [26])	0.71	5.69	–	–	–	–
Singh-Miller (Ref. [27])	0.65	5.69	0.90	5.66	1.30	5.26
			AM05			
This work	0.77	5.79	1.09	5.75	1.59	5.35
			Experiment			
Measurement	1.03	6.10	–	5.82	–	5.35
Reference	[49]	[19]		[50]		[51]

become dominant in larger (1 × N) missing row reconstructions, such as the (1 × 8) depicted in Fig. 4(c).

The homology of these missing row reconstructions on the (110) surface to the (111) surface is illustrated in Fig. 4(c). The (110) missing row reconstruction reveals an homologous mapping from the unreconstructed (110) surface to the (111) surface on the terraces, with the proviso that atoms in the top *two* layers of the (110) surface are drafted into making the mapping.

Standard convention counts only the top atomic layer, one atom per (1 × 1) cell of the ideal (110) surface. With this convention, the (110) is a high-energy surface, as plotted earlier in Fig. 3. However, using this insight concerning a homologous mapping between the (110) and (111) surfaces, the two-atom layer convention is perhaps more physically meaningful, and reveals that the (111) surface and ideal (110) surface energy (labeled as "110/2" in Fig. 3) are competitive.

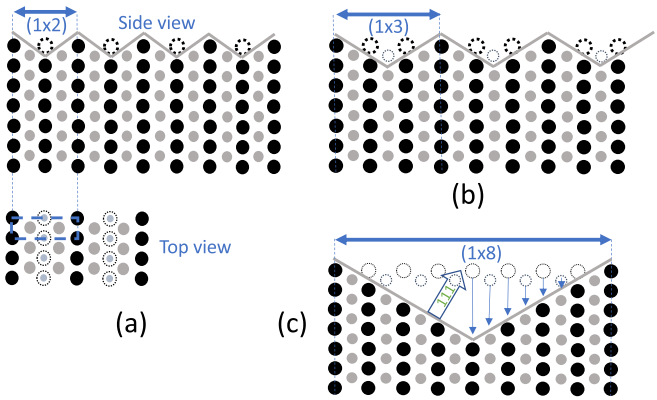

FIG. 4. Schematic of the (110) missing row reconstruction: (a) side view and top view of the (1 × 2) missing row reconstruction, where a line of surface atoms (dotted) is removed from the ideal (1 × 1)-(110) surface. (b) Side view of the (1 × 3) missing row reconstruction. (c) Side view of the larger (1 × 8) missing row reconstruction, where (111) nanoterraces lining the trenches become obvious, and reveal a homologous mapping between the ideal (110) surface and (111) surface, under the condition that the top two layers of atoms on the (110) surface are denoted as surface atoms.

Computational studies of Pt(110) surface structure have been very few. Classical EAM (embedded atoms method) potentials for Pt [57] determined that the (1 × 2) missing row reconstruction was clearly more stable than the ideal surface [58,59], but, lacking explicit consideration of the electronic structure of the surface, this simple computational approach could not confidently resolve the smaller energy differences between this and larger missing row reconstructions. Computational accuracy has not advanced beyond a recent DFT study, which similarly was unable to resolve the relative stability of $N = 2, 3, 4$ missing row reconstructions to within the accuracy of their calculations [60]. Using the greater precision and relative accuracy offered by the slab-consistent bulk reference approach [17], we construct a computational model than can more reliably resolve subtle energy difference among these and even larger (1 × N) missing row reconstructions.

Constructing a viable computational model for a missing row reconstructed surface is more complicated than for the flat unreconstructed surfaces. The missing row models carve deep troughs into the slab along (111) nanoterraces, nominally reducing the thickness—and accuracy—of a slab model of a surface. To mitigate this, the slab model duplicates the missing row structure on the other side of the slab, as illustrated in Fig. 5.

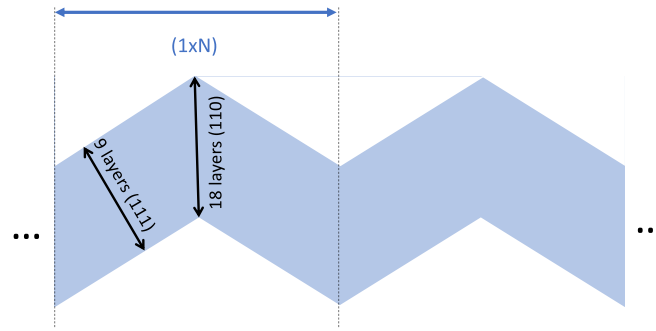

FIG. 5. Slab model for a (1 × N)-(110) missing row reconstruction. As the (111) nanoterraces get wider with increasing N, the model becomes a zigzag structure of (111) slabs with kinks. To map onto a minimally sufficient 9 layer thick (111) slab (in the limit of large N) requires a baseline (110) slab with 18 layers.

To extend the missing row reconstruction, the (111) nanoterraces are widened. As N gets larger, this (110)-oriented slab becomes a series of alternately tilted (111) slabs connected at kinks defined by the ridges and trenches. These (111) spans have half the number of atomic layers as the (conventionally counted) baseline (110) slab from which this model is derived. If at least 9 layers are required to (safely) converge the surface properties of a (111) surface properties from a (111) slab that mandates (at least) 18 atomic layers be used in the baseline (111) slab. In our calculations of missing row reconstructions, we use this 18-layer baseline (110) slab to create the models. While this might be overly sufficient for converging a (110) surface calculation, this provides the minimally sufficient 9 layers in the (111) regions of the model, so as to converge the total surface energy calculation in those (111) regions to within the 0.01 eV/atom uncertainty (as assessed above).

Additional numerical uncertainties can arise for calculations of surface energies of reconstructions of a different extent, because of inequivalent effective k-point samplings. In the calculations described in Sec. V B, we had used k-samplings $k_A \times k_B = 6 \times 4$, 8×6, 10×7, 12×8, 14×10, and 17×12 for the primitive (1×1)-(110) surface cells. The k-limit surface energy (for the 8×6 k grids and greater) converged to 1.594 ± 0.015 eV/(1×1) atom or 0.797 ± 0.007 eV/homologous-surface atom. This 7 meV uncertainty is an overall uncertainty due to the k resolution. This could potentially be magnified when considering relative energies of larger $(1 \times N)$ reconstructions with inequivalent k sampling, compromising the accuracy of any energy comparisons.

A $k_A \times k_B$ k grid in the (1×1) primitive cell is formally equivalent to a $k_A \times (k_B/N)$ k grid in a $(1 \times \mathrm{N})$ slab unit cell. With the operational constraint that k_B/N must be exactly an integer, different $(1 \times N)$ cells factored from necessarily different k-gridded baseline supercells will generally be afflicted with the full k-limit uncertainties, of roughly the magnitude needed to resolve the energy difference between different-sized reconstructions. We mitigate this uncertainty by renormalizing the surface in different sized supercells to the energy of the (1×2) missing row reconstruction computed in that slab model. A (1×2) missing row reconstruction can be periodically replicated in a $(1 \times 2M)$ supercell, and then this formation energy used to recalibrate all other missing row reconstructions in that $(1 \times 2M)$ slab model. This mostly eliminates k-limit errors in relative energies of different size reconstructions. For example, in the following we use a k-grid equivalent to a 17×12 in a (1×1) supercell to obtain (1×2), (1×3), (1×4), (1×6), and (1×12) missing row reconstructions in a (1×12) supercell, the 14×10-equivalent grid in a (1×10) supercell to recalibrate the (1×10) missing row to the (1×2) missing row [and verify the (1×5) missing row], and adding a 17×14-equivalent k grid to investigate the 7×1 and 14×1 reconstructions.

Figure 6 plots the surface formation energy for missing row reconstructions of increasing size, from the relaxed, unreconstructed (1×1)-(110) surface, up to (1×14) missing row reconstructions with (111) nanoterraces 14 atoms wide.

The (1×2) missing row reconstruction is unmistakably favored over the unreconstructed (1×1)-(110) surface, by almost 50 meV, consistent with the field-ion microscopy images by Kellogg [10] and ion scattering results of Fenter and Gustafsson [53]. The (1×3) missing row reconstruction is lower yet, by another 5 meV/atom. The (1×4) returns upwards to slightly above the (1×2).

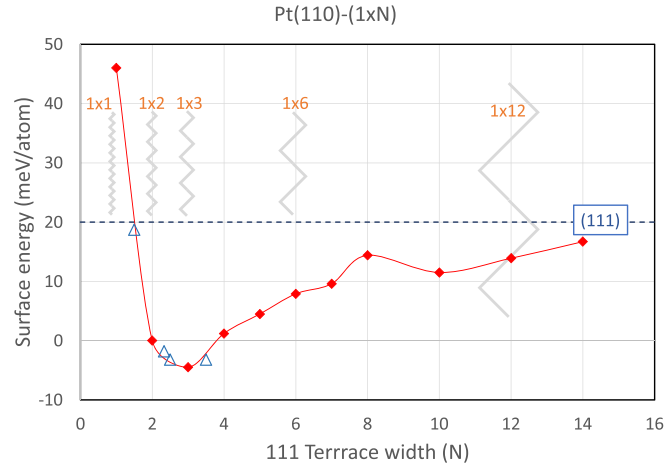

FIG. 6. Relative energies of $(1 \times N)$ missing row reconstructions of the Pt(110) surface, per homologous surface atom, 2 atoms/(1×1)-(110), relative to the (1×2) reconstruction. The dashed (blue) line marks the asymptotic large-N limit of the surface energy computed for a flat (111) surface, which carries a numerical uncertainty of ~10 meV with respect to the energies for the (110) reconstructions plotted here. The triangles plot the energies of composite missing row reconstructions (see text), as a function of the average terrace width of that reconstruction.

Experimental evidence exists for a (1×3) missing row reconstruction on Pt(110) [9,11], although the controversy whether this is stabilized by the presence of impurities remains unresolved [56,61]. The current results support the interpretation that the (1×3) missing row reconstruction is the most stable missing row reconstruction, and that impurities are not necessary to stabilize this reconstruction. While the 5 meV margin favoring it over the (1×2) missing row may not be definitive (to within an uncertainty that could be reasonably asserted), the (1×3) is definitively competitive with the (1×2) missing row [as is the (1×4)]. This supports the hypothesis that the larger scale (1×5), (1×7), (1×9) reconstructions on the Pt(110) surface are composites of (1×3) and (1×2) missing row stripes [56].

An alternate (1×3) structure where the bottom row of the trough is filled proves to be 23 meV/atom higher than the full missing trough structure (as is its complement, where the top ridge row is removed). This also can be thought of as a pair of 2-wide (111) nanoterraces alternating with a pair of 1-wide (111) nanoterraces, for an average 1.5-width nanoterrace. Within this view, the energy for this (1×3) in Fig. 6 is seen to be between the (1×2) missing row and the (1×1) unreconstructed surface (plotted as the triangle in Fig. 6 at $N = 1.5$).

A (1×5) alternative as a composite of a (1×3) and (1×2) missing row troughs [or its complement as (1×3) and (1×2) added-row ridges] has an average 2.5-width terrace. These composite (1×5) reconstructions are 8 meV/atom

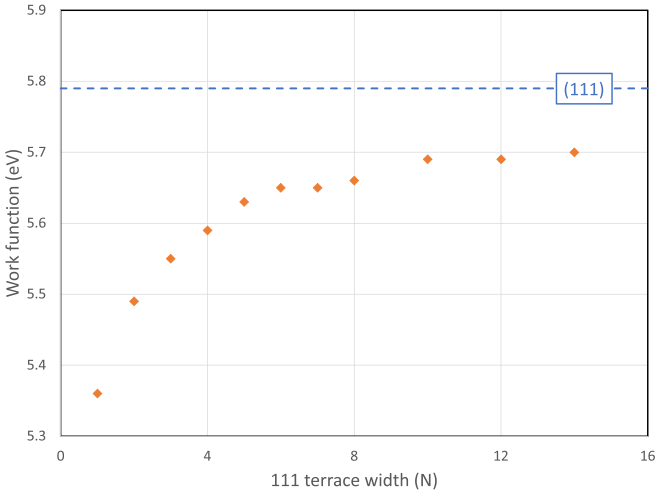

FIG. 7. Computed work functions for Pt(110)-(1 × *N*) missing row reconstructions.

more stable than the full (1 × 5) missing row model with 5-wide nanoterraces, and are intermediate between the (1 × 3) and (1 × 2) missing row structures in Fig. 6. Similarly, the (1 × 7) can be constructed as either a (1 × 3) and two (1 × 2) troughs (or its complement as ridges) with an average nanoterrace width of 2.33, or as a composite of (1 × 4) and (1 × 3) troughs (or ridges) with $N_{ave} = 3.5$. Both of these composites are more stable than the full (1 × 7) missing row trough (by 12 and 11 meV, respectively), and are once more intermediate between the full (1 × 3) minimum and its neighbors. This supports the interpretation of Gritsch *et al.* of the appearance of the (1 × 5) and (1 × 7) reconstructions as composite reconstructions that are intermediate between a transition from a (1 × 2) to a (1 × 3). The dominant aspect in the stability in these reconstructions is the width of the nanoterraces.

Inspection of the asymptotic behavior of the series of (1 × *N*) missing row reconstructions in Fig. 6 reveals that the minimum energy reconstruction at (1 × 3) missing row drifts steadily upwards with increasing (111) nanoterrace width *N*. The widening (111) nanoterraces approach the energy corresponding to the correct asymptotic limit of a monolithic (111) surface energy. This (111)-surface limit (indicated by the dashed line in Fig. 6) is 25 meV/atom below the unreconstructed (1 × 1) surface, but 25 meV above the (1 × 3) missing row reconstruction.

This of large missing row reconstructions drifts to ∼5 meV below the asymptotic limit (111) surface energy. This is well within the roughly 0.01 eV uncertainty in the *k*-limit (111) ideal surface energies determined above. The asymptotic missing row calculation involving expanded (111) terraces and the direct calculation of the (111) surface agree to within an expected precision anticipated by the estimated numerical uncertainties using the slab-consistent bulk reference approach.

In a slab calculation the work function can be straightforwardly extracted as the Fermi level with respect to vacuum. The computed work function for these (1 × *N*) missing row reconstructions, using the AM05 functional and nonlinear core corrections, is presented in Fig. 7.

The work function begins at 5.36 eV for the unreconstructed (1 × 1)-Pt(110) surface, and then monotonically increases with missing row size, converging to 5.69 eV for the largest computed (1 × 14) reconstruction. Just as for the surface energy, this asymptotic value falls short of the direct calculation of the Pt(111) surface (Table II). Unlike the surface energy, this difference in the work function is not a result of model uncertainties. The formation energy of a (1 × *N*) reconstruction is a global average over all the surface atoms, which should trend to the asymptotic (111) surface energy as *N* increases. The work function is a global extremal value: the work function is the lowest energy required to remove an electron from anywhere on the surface. The (111) nanoterraces get ever larger, but the global work function is determined by the global minimum of the "local" work function, which is associated with the ridge and valley kinks in the zigzag of the slab model (Fig. 5).

VI. DISCUSSION

The computations show that the $N = 2$, 3, 4 missing row reconstructions and their nanoterraces are locally stabilized against widening of the (111) nanoterraces. This result provides an additional rationalization for why epitaxially grown Pt on a clean Pt(111) surface can result in triangular, stepped pyramids [20], or thermally grown Pt results in hillocks being formed [21,22]. Previously, kinetic arguments had been invoked to explain the stepped growth [20]. The results here suggest that local total energy arguments also can favor the growth of such stepped, (110) missing rowlike facets.

That the atomically flat Pt(111) surface reconstructs to have an incommensurate compressed quasihexagonal overlayer at elevated temperatures has long been known [13]. Vicinal cuts just slightly away from (111) evolve to alternating stripes of these dense hexagonal overlayers and stepped regions [14]. These steps tend to bunch together to form narrower (111) nanoterraces [15]. This is further evidence supporting the notion of very stable (111) nanoterraces, and is evidence that the commensurate missing row structures are competitive with the incommensurate quasihexagonal (111) reconstruction.

This insight into the nanoscopic morphology of the surface then leads to a possible explanation for the PEEM local work function data exhibited in Fig. 2 for the sputtered Pt surface. The strongly peaked feature at ∼5.7 eV in the data corresponds well with the range that one might expect for the (1 × 2) through (1 × 4) missing row reconstructions, as plotted in Fig. 7, about 5.5–5.6 eV. This is good quantitative agreement, particularly in light of the underestimate of the limit (111) work function computed in Table II (for AM05 and PBE; LDA appears to do better) in comparison to the experimentally determined (111), 6.1 eV [19].

VII. CONCLUSIONS

Leveraging the numerical accuracy enabled by the slab-consistent bulk reference method developed in the previous paper [17], a structural energy was used to reliably resolve subtle energy differences between different Pt(110) surface

reconstructions. The (1×3) missing row reconstruction was found to be the lowest energy, slightly more stable than the (1×2) and (1×4) missing row reconstructions. Within an homology identified between (110) and (111) surface limits via missing row reconstructions on the (110), the computed larger missing row reconstruction energies properly converge to the asymptotic limit of the (111) surface energy. Larger $1 \times N$ reconstructions, such as the 1×5 and 1×7 patterns observed by Gritsch *et al.*, prefer structures that are composites of these smaller missing row structures with narrower (111) nanoterraces. The (111) nanoterraces composing the (110) missing row reconstructions prefer not to widen, indicating a local stability in these features, and support the notion that narrow (111) terraces should be common features on a roughened thermally grown Pt. The inspiration of this effort was to obtain greater understanding of features in the nanoscale surface morphology of sputtered polycrystalline Pt films with (111)-oriented grains leading to morphology of the local work function, so as to gain preliminary insight into electron emission and ultimately into the initiation of electrical breakdown. The computed results for the work functions of these reconstructed surfaces are broadly consistent with the PEEM measurements of local work functions on these thin Pt films.

ACKNOWLEDGMENTS

We thank Paul Clem and Matt Hopkins for many helpful interactions during the course of this project. I (P.A.S.) acknowledge many illuminating discussions with Peter J. Feibelman regarding the modeling of metal surfaces and the physics of platinum surfaces. I am immensely grateful to Ann E. Mattsson for many instructive discussions concerning density functionals and functional development and also for implementing the AM05 functional used in this study into the SEQQUEST code. This work was supported by a Sandia Laboratory Directed Research and Development (LDRD) project. Part of the work was performed at the Center for Integrated Nanotechnologies, a US Department of Energy (DOE) Office of Science User Facility. Sandia National Laboratories is a multimission laboratory managed and operated by National Technology and Engineering Solutions of Sandia, LLC., a wholly owned subsidiary of Honeywell International, Inc., for the US Department of Energy's National Nuclear Security Administration under Contract No. DE-NA0003525. This paper describes objective technical results and analysis. Any subjective views or opinions that might be expressed in the paper do not necessarily represent the views of the US Department of Energy or the United States Government.

[1] R. H. Fowler and L. Nordheim, Electron emission in intense electric fields, Proc. R. Soc. London Ser. A **119**, 173 (1928).

[2] E. L. Murphy and R. H. Good Jr., Thermionic emission, field emission, and the transition region, Phys. Rev. **102**, 1464 (1956).

[3] K. L. Jensen, Electron emission theory and its application: Fowler-Nordheim equation and beyond, J. Vac. Sci. Technol. B **21**, 1528 (2003).

[4] R. G. Forbes and J. H. B. Deane, Comparison of approximations for the principal Schottky-Nordheim barrier function $v(f)$, and comments on Fowler-Nordheim plots, J. Vac. Sci. Technol. B **28**, C2A33 (2010).

[5] M. Berg, S. Smith, D. Scrymgeour, M. Brumbach, P. Lu, S. Dickens, J. Michael, T. Ohta, E. Bussmann, H. P. Hjalmarson, P. A. Schultz, P. G. Clem, M. M. Hopkins, and C. H. Moore, Correlating local work functions with nanoscale surface structure of polycrystalline Pt thin films (unpublished).

[6] H. B. Lyon and G. A. Somorjai, Low-energy electron-diffraction study of the clean (100), (111), and (110) faces of platinum, J. Chem. Phys. **46**, 2539 (1967).

[7] D. Gibbs, G. Grübel, D. M. Zehner, D. L. Abernathy, and S. G. J. Mochrie, Orientational Epitaxy of the Hexagonally Reconstructed Pt(001) Surface, Phys. Rev. Lett. **67**, 3117 (1991).

[8] D. L. Abernathy, S. G. J. Mochrie, D. M. Zehner, G. Grübel, and D. Gibbs, Orientational epitaxy and lateral structure of the hexagonally reconstructed Pt(001) and Au(001) surfaces, Phys. Rev. B **45**, 9272 (1992).

[9] M. Salmerón and G. A. Somorjai, A LEED-AES study of the reconstructed Pt(110) surface and the effect of oxygen treatment, Surf. Sci. **91**, 373 (1980).

[10] G. L. Kellogg, Direct Observations of the (1×2) Surface Reconstruction on the Pt(110) Plane, Phys. Rev. Lett. **55**, 2168 (1985).

[11] P. Fery, W. Moritz, and D. Wolf, Structure determination of the (1×2) and (1×3) reconstructions of Pt(110) by low-energy electron diffraction, Phys. Rev. B **38**, 7275 (1988).

[12] R. J. Needs, M. J. Godfrey, and M. Mansfield, Theory of surface stress and surface reconstruction, Surf. Sci. **242**, 215 (1991).

[13] A. R. Sandy, S. G. J. Mochrie, D. M. Zehner, G. Grübel, K. G. Huang, and D. Gibbs, Reconstruction of the Pt(111) Surface, Phys. Rev. Lett. **68**, 2192 (1992).

[14] M. Yoon, S. G. J. Mochrie, D. M. Zehner, G. M. Watson, and D. Gibbs, Periodic step-bunching on a miscut Pt(111) surface, Surf. Sci. **338**, 225 (1995).

[15] S. Gallego, C. Ocal, and F. Soria, Surface and bulk reconstruction of Pt(111) 1×1, Surf. Sci. **377-379**, 18 (1997).

[16] M. Bott, M. Hohage, T. Michely, and G. Comsa, Pt(111) Reconstruction induced by Enhanced Pt Gas-Phase Chemical Potential, Phys. Rev. Lett. **70**, 1489 (1993).

[17] P. A. Schultz, First-principles calculations of metal surfaces. I. Slab-consistent bulk reference for convergent surface properties, Phys. Rev. B **103**, 195426 (2021).

[18] C. T. Shelton, P. G. Kotula, G. L. Brennecha, P. G. Lam, K. E. Meyer, J. P. Maria, B. J. Gibbons, and J. F. Ihlefeld, Chemically heterogeneous complex oxide thin films via improved substrate metallization, Adv. Func. Mater. **22**, 2295 (2012).

[19] G. N. Derry and J.-Z. Zhang, Work function of Pt(111), Phys. Rev. B **39**, 1940 (1989).

[20] M. Kalff, P. Šmilauer, G. Comsa, and T. Michely, No coarsening in Pt(111) homoepitaxy, Surf. Sci. **426**, L447 (1999).

[21] W. W. Jung, S. K. Choi, S. Y. Kwoen, and S. J. Yeom, Platinum(100) hillock growth in a Pt/Ti electrode stack for ferroelectric random access memory, Appl. Phys. Lett. **83**, 2160 (2003).

[22] Y.-S. Jeong, H.-U. Lee, S.-A Lee, J. P. Kim, H.-G. Kim, S.-Y. Jeong and C. R. Cho, Annealing affect of platinum-based electrodes on physical properties of PZT thin films, Curr. Appl. Phys. **9**, 115 (2009).

[23] J. C. Boettger, Nonconvergence of surface energies obtained from thin-film calculations, Phys. Rev. B **49**, 16798 (1994).

[24] C. J. Fall, N. Bingelli, and A. Baldereschi, Anomaly in the anisotropy of the aluminum work function, Phys. Rev. B **58**, R7544 (1998).

[25] V. Fiorentini and M. Methfessel, Extracting convergent surface energies from slab calculations, J. Phys. Condens. Matter **8**, 6525 (1996).

[26] J. L. F. Da Silva, C. Stampfl, and M. Scheffler, Converged properties of clean metal surface by all-electron first-principles calculations, Surf. Sci. **600**, 703 (2006).

[27] N. E. Singh-Miller and N. Marzari, Surface energies, work functions, and surface relaxations of low index metallic surfaces, Phys. Rev. B **80**, 235407 (2009).

[28] P. J. Feibelman, Energetics of steps on Pt(111), Phys. Rev. B **52**, 16845 (1995).

[29] P. J. Feibelman, Interlayer Self-Diffusion on Stepped Pt(111), Phys. Rev. Lett. **81**, 168 (1998).

[30] P. A. Schultz, SEQQUEST code (unpublished), see https://dft.sandia.gov/Quest/.

[31] D. R. Hamann, Generalized norm-conserving pseudopotentials, Phys. Rev. B **40**, 2980 (1989).

[32] M. Fuchs and M. Scheffler, Ab initio pseudopotentials for electron structure calculations of polyatomic systems using density functional theory, Comput. Phys. Commun. **119**, 67 (1999).

[33] S. G. Louie, S. Froyen, and M. L. Cohen, Nonlinear ionic pseudopotentials in spin-density-functional calculations, Phys. Rev. B **26**, 1738 (1982).

[34] J. P. Perdew and A. Zunger, Self-interaction correction to density-functional approximations for many-electron systems, Phys. Rev. B **23**, 5048 (1981).

[35] J. P. Perdew, K. Burke, and M. Ernzerhof, Generalized Gradient Approximation Made Simple, Phys. Rev. Lett. **77**, 3865 (1996).

[36] R. Armiento and A. E. Mattsson, Functional designed to include surface effects in self-consistent density functional theory, Phys. Rev. B **72**, 085108 (2005).

[37] M. J. Mehl, Occupation-number broadening schemes: Choice of "temperature", Phys. Rev. B **61**, 1654 (2000).

[38] A. E. Mattsson, P. A. Schultz, M. P. Desjarlais, T. R. Mattsson, and K. Leung, Designing meaningful density functional theory calculations in materials science—A primer, Model. Simul. Mater. Sci. Eng. **13**, R1 (2005).

[39] D. D. Johnson, Modified Broyden's method for accelerating convergence in self-consistent calculations, Phys. Rev. B **38**, 12807 (1988).

[40] M. J. Mehl, Pressure dependence of the elastic moduli in aluminum-rich Al-Li compounds, Phys. Rev. B **47**, 2493 (1993).

[41] F. Birch, Finite strain isotherm and velocities for single-crystal and polycrystalline NaCl at high pressures and 300 K, J. Geophys. Res. **83**, 1257 (1978).

[42] F. D. Murnaghan, Finite Deformations of an elastic solid, Am. J. Math. **59**, 235 (1937).

[43] J. W. Arblaster, Crystallographic properties of platinum, Platinum Metals Rev. **41**, 12 (1997).

[44] R. E. McFarlane, J. A. Rayne, and C. K. Jones, Anomalous temperature dependence of shear modulus c_{44} for platinum, Phys. Lett. **18**, 91 (1965).

[45] P. Haas, F. Tran, and P. Blaha, Calculation of the lattice constant of solids with semilocal functionals, Phys. Rev. B **79**, 085104 (2009).

[46] S. Kurth, J. P. Perdew, and P. Blaha, Molecular and solid-state tests of density functional approximations: LSD, GGAs, and meta-GGAs, Int. J. Quantum Chem. **75**, 889 (1999).

[47] A. E. Mattsson, R. Armiento, J. Paier, G. Kresse, J. M. Wills, and T. R. Mattsson, The AM05 density functional applied to solids, J. Chem. Phys. **128**, 084714 (2008).

[48] R. J. Magyar, A. E. Mattsson, and P. A. Schultz, Some practical considerations for density functional theory studies of chemistry at metal surfaces, in *Metallic Systems: A Quantum Chemist's Perspective*, edited by T. Allison, O. Coskuner, and C. A. Gonzalez (CRC, Taylor and Francis, Boca Raton, FL, 2011), p. 163.

[49] W. R. Tyson and W. A. Miller, Surface free energies of solid metals: Estimation from liquid surface tension measurement, Surf. Sci. **62**, 267 (1977).

[50] M. Salmorón, S. Ferrer, M. Jazzar, and G. A. Somorjai, Photoelectron-spectroscopy study of the electronic structure of Au and Ag overlayers on Pt(100), Pt(111), and Pt(997) surfaces, Phys. Rev. B **28**, 6758 (1983).

[51] R. Vanselow and X. Li, The work function of kinked areas on clean, thermally rounded Pt and Rh crystallites: Its dependence on the structure of terraces and edges, Surf. Sci. **264**, L200 (1992).

[52] D. R. Jennison, P. A. Schultz, D. B. King, and K. R. Zavedil, BaO/W(111) thermionic emitters and the effects of Sc. Y, La, and the density functional used in the computations, Surf. Sci. **549**, 115 (2004).

[53] P. Fenter and T. Gustafsson, Structural analysis of the Pt(110)-(1 × 2) surface using medium-energy ion scattering, Phys. Rev. B **38**, 10197 (1988).

[54] E. Vlieg, I. K. Robinson, and K. Kern, Relaxation in the missing-row structure of the (1 × 2) reconstructed surfaces of Au(110) and Pt(110), Surf. Sci. **233**, 248 (1990).

[55] I. K. Robinson, P. J. Eng, C. Romainczyk, and K. Kern, X-ray determination of the 1 × 3 reconstruction of the Pt(110), Phys. Rev. B **47**, 10700 (1993).

[56] T. Gritsch, D. Coulman, R. J. Behm, and G. Ertl, A scanning tunneling microscopy investigation of the structure of the Pt(110) and Au(110) surfaces, Surf. Sci. **257**, 297 (1991).

[57] S. M. Foiles, M. I. Baskes, and M. S. Daw, Embedded-atom-method functions for the fcc metals Cu, Ag, Au, Ni, Pd, Pt, and their alloys, Phys. Rev. B **33**, 7983 (1986).

[58] M. S. Daw, Calculations of the energetics and structure of Pt(110) reconstruction using the embedded atom method, Surf. Sci. Lett. **166**, L161 (1986).

[59] S. M. Foiles, Reconstruction of fcc (110) surfaces, Surf. Sci. Lett. **191**, L779 (1987).

[60] T. Zhu, S.-G. Sun, R. A. van Santen, and E. J. M. Hensen, Reconstruction of clean and oxygen-covered Pt(110) surfaces, J. Phys. Chem. C **117**, 11251 (2013).

[61] I. K. Robinson, P. J. Eng, C. Romainchyk, and K. Kern, Higher order reconstructions of Pt(110) induced by impurities, Surf. Sci. **367**, 105 (1996).